An Efficient Approach to Texture-Based Image Retrieval

Mahmoud R. Hejazi, Yo-Sung Ho

Department of Information and Communications, Gwangju Institute of Science and Technology (GIST), 1 Oryong-dong, Buk-gu, Gwangju 500-712, South Korea

Received 19 April 2007; accepted 15 October 2007

ABSTRACT: In this article, we present an efficient approach for image retrieval based on the textural information of an image, such as orientation, directionality, and regularity. For this purpose, we apply the nonlinear modified discrete Radon transform to estimate these visual contents. We then utilize texture orientation to construct the rotated Gabor transform for extraction of the rotation-invariant texture feature. The rotation-invariant texture feature, directionality, and regularity are the main features used in the proposed approach for similarity assessment. Experimental results on a large number of texture and aerial images from standard databases show that the proposed schemes for feature extraction and image retrieval significantly outperform previous works, including methods based on the MPEG-7 texture descriptors. © 2008 Wiley Periodicals, Inc. Int J Imaging Syst Technol, 17, 295–302, 2007; Published online in Wiley InterScience (www.interscience.wiley.com). DOI 10.1002/ima.20120

Key words: content-based image retrieval; invariant texture analysis; nonlinear modified discrete Radon transform; texture descriptors

I. INTRODUCTION

With the advancement of multimedia technologies, a huge number of multimedia information, such as images and videos are available worldwide, and efficient multimedia retrieval systems are an inevitable need for many applications. In this article, we address the problem of content-based image retrieval (CBIR) that has been an active and fast advancing research area for more than one decade. Despite remarkable progress in both theoretical research and system development, there are still many challenging problems in this area that continue to attract researchers from multiple disciplines (Smeulders et al., 2000).

A CBIR system utilizes visual contents to search images from digital image databases based on a user's query (e.g. an example image). Visual contents (or features) of an image, such as color, shape, texture, and spatial layout are used to represent and index an image. Among them, texture is one of the most important ones, due to its presence in most real and synthetic world images, which makes it under high attention not only for CBIR but also for many other applications in computer vision, medical imaging, remote sensing, and so on.

There are a variety of approaches for texture analysis, however in the majority of existing works; it is assumed that all images are acquired from the same orientation. This assumption is not realistic in practical applications, where images may be taken with different rotation, scale, etc. There are numerous methods proposed for addressing the problem of the rotation invariant texture analysis (Zhang and Tan, 2002). Among them, some use rotation invariant models to solve this problem (Haley and Manjunath, 1999; Pun and Lee, 2003), though, a majority attempt to estimate the directional information in an image and use it with other tools, such as wavelets to perform rotation-invariant analysis (Jafari-Khouzani and Soltanianzadeh, 2005; Hejazi and Ho, 2006).

However, most approaches proposed for texture analysis are not applicable for actual image retrieval. First, many approaches are dataset-dependent and need to be trained for each dataset individually before applying for image retrieval (Haley and Manjunath, 1999; Jafari-Khouzani and Soltanianzadeh, 2005). Second, the performance of most approaches is degraded when the level of directionality and/or regularity is decreased (Manjunath et al., 2000; Lee and Chen, 2005). Last but not least, although the response time is a key factor in most image retrieval applications, the invariant feature extraction is a time-consuming process in most existing texture analysis methods.

Here, we apply the second modified Radon transform (Hejazi et al., 2006), which is referred to as the nonlinear modified discrete Radon transform (NLMDRT) in this article, and is a fast and efficient transform for analysis of directional information, to estimate the texture orientation, directionality, and regularity. We also utilize the rotated Gabor transform (Hejazi and Ho, 2007) to extract the rotation-invariant texture feature. Using these features, we finally propose an efficient mechanism for CBIR and examine it through some applications.

The rest of the article is organized as follows. In Section II, we briefly introduce NLMDRT, and present schemes for extraction of textural information from an image using NLMDRT. Then, in Section III, we propose our approach for image retrieval. Section IV provides some applications of the proposed mechanism and presents experimental results. Finally, conclusions are given in Section V.

Correspondence to: Mahmoud R. Hejazi; e-mail: m_hejazi@gist.ac.kr or Yo-Sung Ho; e-mail: hoyo@ gist.ac.kr

Grant sponsors: IITA, MIC through RBRC at GIST, and MOE through the BK21 project.

II. EXTRACTION OF TEXTURAL INFORMATION

A. NLMDRT. NLMDRT is the second modified version of the conventional discrete Radon transform, a fast and efficient tool for rotation estimation in an image that we proposed in a previous paper (Hejazi et al., 2006). To define NLMDRT, we start with the Radon transform, which is the projection of the image intensity along a radial line oriented at a specific angle. The continuous Radon transform of a 2D image is defined as

$$R(\rho,\theta)=\int_{-\infty}^{\infty} f(\rho\cos\theta - s\sin\theta, \rho\sin\theta + s\cos\theta)ds, \qquad (1)$$

where ρ is the smallest distance from the origin, and θ is its angle with the x-axis. The discrete Radon transform of a 2D digital image $g(m,n)$ of size $M \times N$ can then be approximated from Eq. (1) as

$$R(\rho_r,\theta_t)\approx \Delta s\cdot \sum_{k=0}^{S_{\rho,\theta}-1} g(x'_k,y'_k), \qquad (2)$$

where

$$\begin{aligned} x'_k &= [\rho_r\cdot\cos\theta_t - s_k\cdot\sin\theta_t - x_{\min}],\\ y'_k &= [\rho_r\cdot\sin\theta_t + s_k\cdot\cos\theta_t - y_{\min}], \end{aligned} \qquad (3)$$

and $[\cdot]$ represents the rounding operation. Note that in Eqs. (2) and (3), the discrete variables are provided by proper sampling of continuous variables in Eq. (1) (Hejazi et al., 2006).

We define the set $\Phi_{r,t}$ as

$$\Phi^{r,t}=\{g(x'_i,y'_i):\ \rho=\rho_r,\theta=\theta_t,\quad i=0,1,\ldots,S_{\rho,\theta}-1\}, \qquad (4)$$

and Ψ^t as a set of successive concatenations of the sets $\Phi^{r,t}|r=0,1,\ldots,P_\theta-1$ and $\theta=\theta_t\}$:

$$\Psi^t=\mathrm{Concat}(\Phi^{r,t}),\quad r=0,1,\ldots,P_\theta-1 \quad\text{and}\quad \theta=\theta_t. \qquad (5)$$

NLMDRT is then defined as

$$R_{\mathrm{MM}}(\lambda_j,\theta_t)\equiv \Delta s\cdot\ \mathrm{Mean}(\psi^t_j),\quad j=0,1,\ldots,M-1, \qquad (6)$$

where

$$\lambda_j=\lambda_{\min}+j,\quad j=0,1,\ldots,M-1,\quad\text{and}\quad \lambda_{\min}=-(M-1)/2. \qquad (7)$$

The good performance of NLMDRT in direction estimation motivates us to utilize it for the extraction of other textural information from an image. In the following subsections, we present schemes for the estimation of orientation, directionality, and regularity.

B. Orientation Estimation. There are a variety of techniques in the literature to estimate orientation, including methods using image gradients and signal autocorrelation structure (Mester, 2000), the angular distribution of signal power in the Fourier domain (Bigun et al., 1991; Chandra, 1998), directional histograms (Manjunath et al., 2000), and the discrete Radon transform (Jafari-Khouzani and Soltanianzadeh, 2005; Hejazi and Ho, 2006).

Here, we use NLMDRT whose performance is significantly better than the conventional discrete Radon transform in direction estimation (Hejazi et al., 2006), to achieve this goal. For this purpose, we first calculate the variance array of an image as

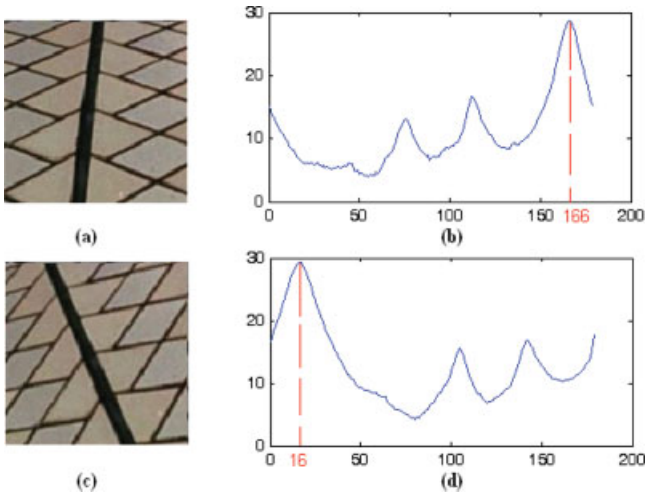

Figure 1. Variance arrays of an anisotropic image for two different orientations. (a) original image, (b) variance array of the original image, (c) a 30°-rotated version of the image, and (d) variance array of the rotated image. [Color figure can be viewed in the online issue, which is available at www.interscience.wiley.com.]

$$S_{R_{\mathrm{MM}}}(\theta)=\mathrm{Var}_{\theta_t\in[0,180)}[R_{\mathrm{MM}}(\rho_r,\theta_t)]. \qquad (8)$$

where R_{MM} is NLMDRT of the image as defined in Eq. (6) and is calculated for all directions with θ_t from 0 to 179° with step size 1°.

Defining the dominant direction D_a as the direction with more straight lines (and in general more directionality), we expect the variance array to have a global maximum at the direction perpendicular to D_a. Thus, D_a is defined as

$$D_\alpha=\mathrm{argmax}_{\theta_t}(S_{R_{\mathrm{MM}}})-90^\circ. \qquad (9)$$

This point can be easily verified for the multidirectional anisotropic texture in Figure 1. As shown, there is a peak for each main direction of the image. Using this idea, we can even define some principal direction(s) for isotropic images (Fig. 2), because in the real world pure isotropicity rarely occurs.

Additionally, because images of a scene are supposed to take from different orientations, we may apply NLMDRT to a disk shape area from the middle of images to increase the accuracy of the estimation.

C. Directionality Estimation. Although the texture directionality is sometimes referred to the dominant direction of a texture (Manjunath et al., 2000; Lee and Chen, 2005), here we use a more general definition of directionality that is applied to determine the level of anisotropicity (or isotropicity) in an image (Tamura et al., 1978).

We first examine the examples of Figures 1 and 2 to see the effect of directionality in the variance array of an image. For the multidirectional texture of Figure 1, we can see that principal directions are well separated from other peaks in the variance array. However, for the isotropic texture, the variance array has a noisy-shape figure, and there are many peaks with close values to the

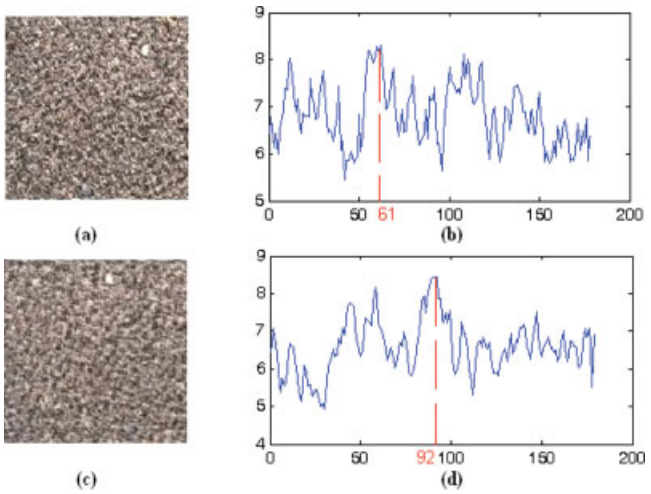

Figure 2. Variance arrays of an isotropic image for two different orientations. (a) original image, (b) variance array of the original image, (c) a 30°-rotated version of the image, and (d) variance array of the rotated image. [Color figure can be viewed in the online issue, which is available at www.interscience.wiley.com.]

maximum peak (Fig. 2). We now generalize this result through some more examples.

Figure 3 shows three different scales of another anisotropic image and their variance arrays. As it can be easily seen in Figure 3, all variance arrays have a clear dominant direction (or peak) around 100° and their general shapes are almost the same. However, the peak widths of the dominant directions are different for each figure. Here, a peak width is defined as the distance between each side of a peak on its corresponding DC-bias line (i.e., Mean($S_{R_{MM}}$)). From Figure 3, it can be easily seen that coarser images have greater peak widths.

We now examine the same problem in an isotropic image. Figure 4 shows three different scales of an isotropic image and their variance arrays. As shown in Figure 4, the shapes of variance arrays are no longer similar; however, all have noisy-shape figures, especially when the level of coarseness is decreased. Consequently, there are many peaks above DC-bias lines with close values to each other.

Furthering the analysis, we can conclude that in pure anisotropicity (directionality), there is only one peak, and in pure isotropicity (nondirectionality), there are no peaks in the variance array. To this end, we define the directionality d_{iso} as

$$d_{\text{iso}} = \begin{cases} 1, & N_p = 0 \quad \text{or} \quad N_p > N_{\text{iso}}, \\ 1, & N_p = 1 \quad \text{and} \quad \beta_D > \beta_{\text{iso}}, \\ (N_p - 1)/N_{\text{iso}}, & \text{otherwise}, \end{cases} \tag{10}$$

where N_p is the number of peaks in the variance array above its DC-bias line, β_D is the peak width of the dominant direction, and N_{iso} and β_{iso} are the two thresholds, which control the level of isotropicity. In this work, we set N_{iso} and β_{iso} to 8 and 90°, respectively.

Additionally, because there is potential for overestimation of the number of peaks, it is also recommended that the variance array passes through a smoother to remove the undesired noisy-type peaks. From Eq. (10), it can be easily seen that small values of d_{iso} show anisotropic dominancy, and larger values emphasize on isotropicity. For extreme cases, i.e. anisotropic textures with one dominant direction and pure isotropic textures, d_{iso} is 0 and 1, respectively.

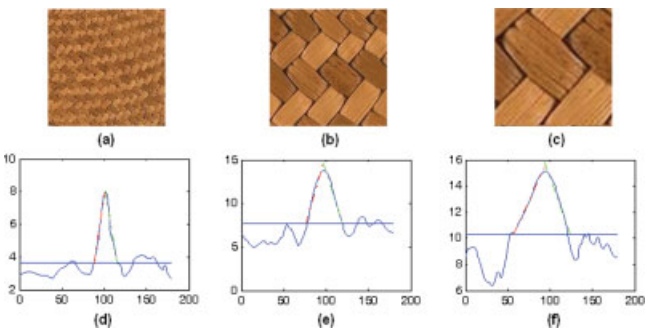

Figure 3. Variance arrays of an anisotropic image for different scales. [Color figure can be viewed in the online issue, which is available at www.interscience.wiley.com.]

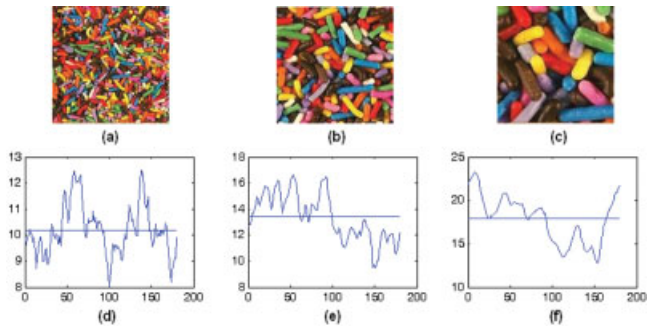

Figure 4. Variance arrays of an isotropic image for different scales. [Color figure can be viewed in the online issue, which is available at www.interscience.wiley.com.]

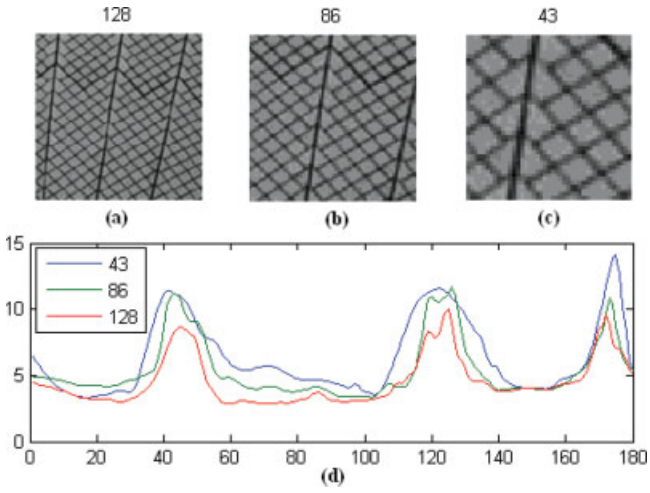

Figure 5. Estimating regularity. (a) image I (and subimage I_1) of size 128 × 128, (b) subimage I_2 of size 86 × 86, (c) subimage I_3 of size 43 × 43, (d) variance arrays of three subimages. [Color figure can be viewed in the online issue, which is available at www.interscience.wiley.com.]

Table I. Calculation of similarity values in the example of Figure 5.

Subimages I_1 and I_2	Subimages I_1 and I_3	Subimages I_2 and I_3
$N_p^1 = 4, N_p^2 = 4, m = 4$	$N_p^1 = 4, N_p^3 = 4, m = 3$	$N_p^2 = 4, N_p^3 = 3, m = 3$
$P_{mat}^1 = \{44, 119, 125, 172\}$	$P_{mat}^g = \{44, 119, 172\}$	$P_{mat}^{g_1} = \{43, 119, 173\}$
$P_{mat}^2 = \{43, 119, 124, 173\}$	$P_{mat}^{g_2} = \{40, 121, 175\}$	$P_{mat}^{g_2} = \{40, 121, 175\}$
$P_{diff} = 0.0083$	$P_{diff} = 0.0111$	$P_{diff} = 0.0111$
SIM(1, 2) = 0.9917	SIM(1, 3) = 0.8476	SIM(2, 3) = 0.8476

D. Regularity Estimation. Another important feature that is used to characterize an image is the texture regularity; regularity determines the level of structuredness in an image, usually estimated by finding periodic patterns in the image. There are some methods in literature for estimation of the regularity (Manjunath et al., 2000; Lee and Chen, 2005); however, these methods are very complex and not significantly efficient, especially when the level of anisotropicity does not attain a required threshold.

In this work, we find this periodicity by comparing variance arrays of blocks of the image. These variance arrays are expected to be quite similar for a complete regular image. Here, we divide the image into three overlapped blocks, where the first block is the image itself with the size $M \times M$, and the two other blocks are subimages with sizes ($2M/3 \times 2M/3$) and ($M/2 \times M/2$) that are extracted from the middle of the image.

The criterion for similarity measurement is based on the numbers and positions of the peaks in their variance arrays. Therefore, let N_p^i be the number of peaks above the DC-bias line of the variance array of the ith subimage, and $P_{pos}^i(j), j = 1, \ldots, N_p^i$ be positions of these peaks. We can then compare each pair of variance arrays; i.e. the variance arrays of the kth and lth subimages, and calculate their similarity SIM(k,l) based on the number and positions of peaks in P_{pos}^k that have proper matches in P_{pos}^l.

We say that a peak q in P_{pos}^l is a proper match of a peak p in P_{pos}^k if first, q has the minimum position difference with p as compared with other peaks in P_{pos}^l, and second, this difference is less than a threshold T_r. Let us assume that m is the number of peaks in P_{pos}^k that has proper matches in P_{pos}^l, P_{mat}^k, and P_{mat}^l are subsets of P_{pos}^k and P_{pos}^l whose elements are positions of these m peaks in P_{pos}^l and their proper matches in P_{pos}^l. We can then calculate SIM(k,l) as

$$\mathrm{SIM}(k,l) = \left[\frac{2m}{(N_p^k + N_p^l)}\right](1 - P_{diff}), \tag{11}$$

where $[\cdot]$ represents the rounding operation, and

$$P_{dif} = |\overline{P_{mat}^k} - \overline{P_{mat}^l}|/T_r, \quad \text{if } P_{dif} > 1, \quad \text{then set } P_{dif} = 1. \tag{12}$$

Having compared all possible pairs of variance arrays, we calculate regularity r_t as a weighted average of these similarity values, with a bigger weight for subimages with greater sizes:

$$r_t = 0.5\mathrm{SIM}(1,2) + 0.3\mathrm{SIM}(1,3) + 0.2\mathrm{SIM}(2,3). \tag{13}$$

where r_t has a value between 0 and 1 that show irregularity and complete regularity, respectively.

We examine the procedure through the example of Figure 5. A near regular image is shown in Figure 5a and its subimages are in Figures 5b and 5c. Let us refer to these images as I_1, I_2, and I_3, whose variance arrays have peaks at positions {44, 119, 125, 172}, {43, 119, 124, 173}, and {40, 121, 175}, as shown in Figure 5d. We summarize the process of regularity estimation in Table I. Note that in calculation, we set T_R to 30°. Using Eq. (13) and results of Table I, we can estimate r_t as 0.9196. It means that the image of Figure 5a is a near-regular image as expected.

III. TEXTURE-BASED IMAGE RETRIEVAL

Similar to most CBIR systems, we need to index images by extracting their features in an offline process. We then submit a query image and find similar images to that query based on a matching criterion. We first start with feature extraction. Figure 6 represents the block diagram of the proposed scheme for this step. As shown, the system extracts three different features for an image; rotation-invariant texture feature f_{inv}, directionality d_{iso}, and regularity r_t.

We have already presented techniques for the estimation of d_{iso} and r_t in Section II. Note that because all proposed schemes utilize the variance array of NLMDRT of the input image I for their estimation, this part is performed only once, results to the significant reduction of the total computational time.

The other feature is the rotation-invariant texture feature f_{inv}. As it can be seen in Figure 6, after estimating the dominant direction D_a (Section II.B), we use the estimated direction to construct f_{inv}. There are two different ways to perform this task. One way is to rotate the image based on its dominant direction and then calculate

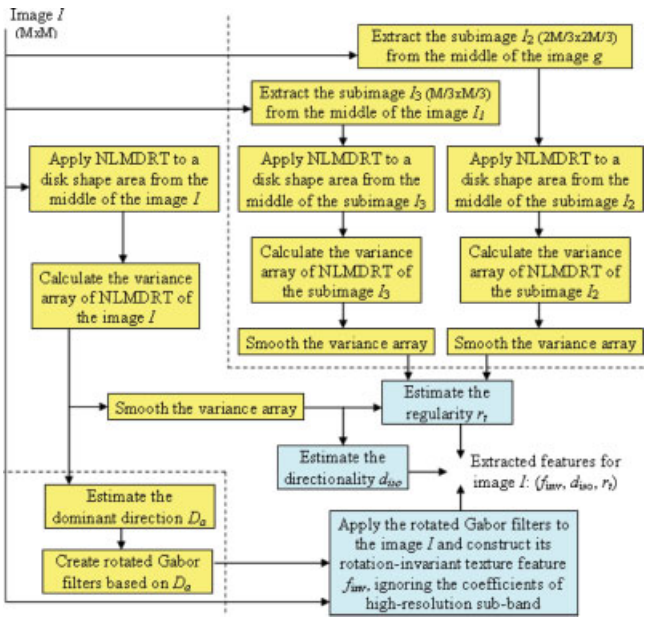

Figure 6. Block diagram of the proposed scheme for feature extraction. [Color figure can be viewed in the online issue, which is available at www.interscience.wiley.com.]

Table II. Performance of orientation estimation in different schemes.

	Proposed Method	Method in Jafari-Khouzani and Soltanianzadeh (2005)	Method in Lee and Chen (2005)	Method in Jalil et al. (2006)
Correct estimation rate (%)	90.8 (8369/9216)	81.0 (7461/9216)	77.3 (7124/9216)	82.4 (7593/9216)
Processing time (s)	0.22	0.51	0.72	0.21

the wavelet transform (Jafari-Khouzani and Soltanianzadeh, 2005). However, this method is not appropriate in general, because we may lose relatively large amounts of data through rotation that consequently decreases the accuracy of the analysis.

Another method, which we use in this work, is based on the definition of the Gabor transform that is a directional wavelet transform (Haley and Manjunath, 1999; Hejazi and Ho, 2006). In this method, we apply the dominant direction in generation of rotated Gabor filters to extract f_{inv}. For this purpose, filters are initially oriented from D_{a}° rather than 0° (Hejazi and Ho, 2007).

Using the proposed scheme, the system can now compare features of the query with features of images in the collection based on some matching criterions. Because three features are used in this work, three matching scores need to be computed. A weighted average of the matching scores is then calculated to get a final score for each image. Finally, we rank images based on these final scores and top-ranked images are displayed to the user as the result of retrieval.

We now explain the process of similarity assessment in detail. The first feature is the rotation-invariant texture feature. To compare two rotation-invariant texture features, we use the Bray–Curtis distance metric, defined as

$$d_{\text{B}}(I_1, I_2) = \frac{\sum_{\text{i}} |f_{1\text{i}} - f_{2\text{i}}|}{\sum_{\text{i}} f_{1\text{i}} + f_{2\text{i}}}, \tag{14}$$

where f_1 and f_2 are the features of images I_1 and I_2.

If we consider a score of 0 for a no-matching scenario and a score of 1 for an exact-matching scenario, the score S_{f} between a query image I_{q} and an image I_{DB} is calculated as

$$S_{\text{f}} = 1 - d_{\text{B}}(I_{\text{q}}, I_{\text{DB}}), \tag{15}$$

where $f_{\text{inv}}^{\text{q}}$ and $P_{\text{inv}}^{\text{DB}}$ are rotation-invariant texture features I_{q} and I_{DB}, respectively.

For the directionality d_{iso} and the regularity r_{t}, scores S_{d} and S_{r} between I_{q} and I_{DB} are calculated as

$$S_{\text{d}} = 1 - |d_{\text{iso}}^{\text{q}} - d_{\text{iso}}^{\text{DB}}|, \tag{16}$$

$$S_{\text{r}} = 1 - |Q(r_{\text{t}}^{\text{q}}) - Q(r_{\text{t}}^{\text{DB}})|, \tag{17}$$

respectively, where d_{iso} and r_{t} are texture directionality and texture regularity features as defined in Eqs. (10) and (13), and $Q(r_{\text{t}})$ is the quantized value of r_{t}, defined as

$$Q(r_{\text{t}}) = \frac{[8r_{\text{t}}]}{8}, \tag{18}$$

The final relevance score S_{FIN} between the images I_{q} and I_{DB} can be then calculated as

$$S_{\text{FIN}} = w_{\text{f}} \cdot S_{\text{f}} + w_{\text{d}} \cdot S_{\text{d}} + w_{\text{r}} \cdot S_{\text{r}}, \quad w_{\text{f}} + w_{\text{d}} + w_{\text{r}} = 1.$$

Computing S_{FIN} for all images in the collection, we select images with the highest scores as top-ranked images. In Section IV.C, we examine an alternative scheme for finding the top-ranked images based on S_{f}, S_{d}, and S_{r}.

IV. EXPERIMENTAL RESULTS

For the evaluation of the proposed schemes, we performed several experiments on a set of images from the VisTex database (VisTex, 2002), including texture images from the Brodatz album (Brodatz, 1966), as well as a variety of nontraditional textures. We also performed experiments on a collection of aerial images that have already been used for the evaluation of the homogeneous texture descriptor in MPEG-7 (Manjunath et al., 2003). Note that all experiments performed on an HP workstation computer with a 3.06 GHz Intel CPU and 2 GB RAM.

A. Orientation Estimation. In the first experiment, we evaluated the proposed scheme in Section II.B for orientation estimation. Here, we used 9792 texture images of size 128 × 128. For generating the dataset, we utilized 144 images of size 512 × 512 from the Vistex database with different textural classes, such as Barks, Clouds, Tiles, and Paintings, and so forth (VisTex, 2002).

Each 512 × 512 image was then divided into four 256 × 256 nonoverlapping blocks, and one 128 × 128 subimage (subclass) was extracted from the middle of each block. To create rotated versions of these subimages, each 256 × 256 block was rotated at angles from 10 to 160° with a step size of 10°, and then one 128 × 128 subimage was selected from the center of each rotated block.

Keeping the 576 nonrotated images as references, we estimated the dominant direction for the remaining 9216 images. Let α_{R} be the rotation angle, and D_0 and $D_{\alpha_{\text{R}}}$ be the dominant directions of the nonrotated and rotated images, respectively. We suppose that the estimation is correct if

$$|\alpha_{\text{R}} - (D_0 - D_{\alpha_{\text{R}}}) \leq 3. \tag{20}$$

Results of estimation have been summarized in Table II. For comparison, we also represent results of some state-of-the-art works for orientation estimation, including the proposed method in Jafari-Khouzani and Soltanianzadeh (2005) that uses the second derivative of the variance of the Radon transform to estimate the orientation; the method presented in Lee and Chen (2005) for estimation of

Table III. Categorization of images based on their texture regularities.

Regularity Range	Category
$0.725 \leq r_{\text{t}} \leq 1$	Regular
$0.475 \leq r_{\text{t}} \leq 0.775$	Near regular
$0.225 \leq r_{\text{t}} \leq 0.525$	Slightly regular
$0 \leq r_{\text{t}} \leq 0.275$	Irregular

Table IV. Performance of regularity estimation in different schemes.

	Proposed Method	Method in Manjunath et al. (2000)	Method in Lee and Chen (2005)
Correct estimation rate (%)	83.5 (8179/9792)	79.6 (7792/9792)	75.3 (7375/9792)
Processing time (s)	0.35	3.19	0.43

direction component in texture browsing descriptor of MPEG-7 (Manjunath et al., 2003) that applies Hough transform on the Fourier spectrum to detect dominant direction; and finally a method based on the principal component analysis (Jalil et al., 2006).

Note that in these experiments, and for the sake of uniformity, all methods have been applied on a disk-shape area from the middle of images instead of the whole image. As it can be easily seen from Table II, the proposed method is not only significantly better than the other methods in orientation estimation but also quite fast.

B. Regularity Estimation. In this experiment, we evaluated the regularity estimation scheme proposed in Section II.D on the dataset of the first experiment. To this end, we determined the regularity category of each image based on the estimated regularity value r_t using Table III. Estimation is supposed to be correct when the estimated category is the same as the actual category.

Table IV shows results for this experiment; the reference work in MPEG-7 that performs a complicated scheme on the autocorrelation functions of sets of projected filtered images to estimate the regularity (Manjunath et al., 2000); and the method in Lee and Chen (2005) that applies the radial wedge distribution on the Fourier spectrum to compute the regularity. It can be seen from Table IV that the proposed method outperforms previous schemes.

C. Retrieval Accuracy. In the third experiment, we examined the accuracy of the proposed image retrieval mechanism with different weight settings for f_{inv}, d_{iso}, and r_t in Eq. (19). We performed this experiment on the dataset of the first experiment, with 9792 images for the image collection. Among them, 576 images (one from each subclass) were used for querying. Figure 7 shows an example of image retrieval for an irregular image with a mixed directionality. As it can be seen in this example, all top-ranked results are relevant answers to this query.

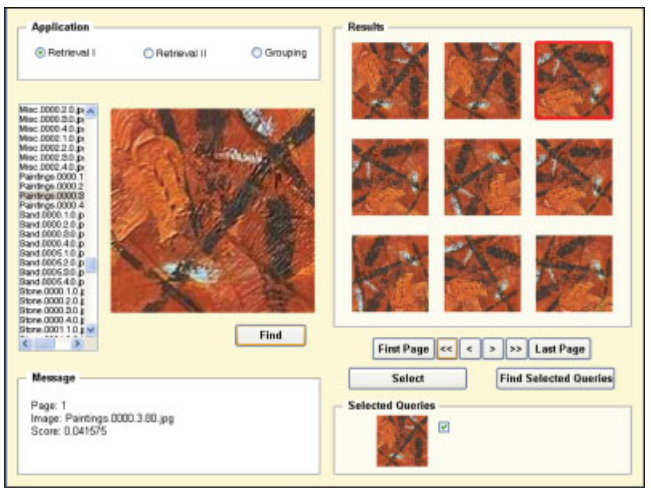

Figure 7. Retrieval results for a typical query image. [Color figure can be viewed in the online issue, which is available at www.interscience.wiley.com.]

In this work, we evaluate the retrieval accuracy for a query based on the precision value defined as

$$\text{Precision} = \frac{N_{REL}}{N_{CAN}}, \tag{21}$$

where N_{REL} is the number of relevant images to the query in N_{CAN} retrieved images. The overall accuracy is calculated by taking the average over precision values of all 576 queries.

In the first step, we retrieved relevant images for a query based on their textural subclasses. In this case, the total number of relevant images in the database is 17 images for each query. The overall accuracy has been drawn in Figure 8 for this experiment, where we only utilized the rotation invariant texture feature f_{inv} for scoring. We can see that the overall accuracy is almost perfect in this experiment, which shows that the proposed approach is well invariant to rotation.

In the next step, relevant images have been retrieved for a query based on their textural classes. In this case, the total number of relevant images in the dataset is 68 images for each query image. Results of this experiment are shown in Table V for different weight settings in Eq. (19).

In this experiment, we also applied an adaptive method for scoring. This method is using this point that when images I_q and I_{DB} have a quite different directionality or regularity feature, the image I_{DB} is not a proper candidate for retrieval. For instance, I_q is well directional, however I_{DB} is isotropic; or I_q is regular, but I_{DB} is irregular.

Therefore, we can set a threshold for maximum acceptable distance (or minimum acceptable score) between the directionality features of I_q and I_{DB}, and another threshold for distance between their regularity features. All images with greater distances (or less scores) than these thresholds are scored to 0. The whole procedure can be summarized as

$$S_{FIN} = \begin{cases} 0, & S_d < 0.5 \quad \text{or} \quad S_r < 0.5, \\ 0.9\,S_f + 0.05\,S_d + 0.05\,S_r & \text{otherwise.} \end{cases} \tag{22}$$

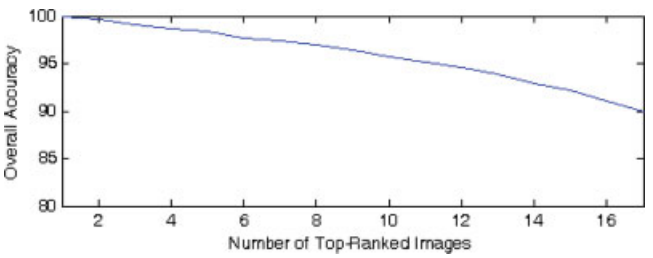

Figure 8. Overall accuracy based on relevance to textural subclasses. [Color figure can be viewed in the online issue, which is available at www.interscience.wiley.com.]

As it can be seen in Eq. (22), we chose small weights for the directionality and regularity features as compared with the rotation-invariant texture feature, because the minimum distance between quantized values of each of those features, which is 0.125 in this work, is quite greater than the minimum distance between two rotation-invariant texture features that may be even less than 0.01. Results in Table V verify this point, where the overall accuracy is higher for settings with smaller weights for the directionality and regularity features.

From Table V, it can be also seen that the adaptive scoring has higher performance, because a large number of irrelevant images are disregarded through the score thresholding of Eq. (22). We can even expect higher accuracy for the system if a more precise categorization scheme is performed; however, because such a process may increase the overall processing time, it is not recommended for applications whose response times have to be short.

D. Partitioning of Aerial Image. In the last experiment, we applied our retrieval scheme for partitioning of aerial images. Remotely sensed data, such as aerial imagery, are an excellent dataset on which to demonstrate another application potential of the rotation-invariant texture feature. Here, we used this approach for the partitioning of such a dataset in this experiment.

For this purpose, we used 220 aerial images of sizes 640 × 640. For each image, the rotation-invariant texture feature is extracted for each nonoverlapping 128 × 128 pixel tiles. Selecting one of tiles as a query, we compute the relevance scores between this tile and all other tiles in the image using Eq. (19), setting weights w_d and w_r to 0.

We then apply a simple agglomerate clustering algorithm to divide the tiles into two clusters based on their relevance scores. The tiles that are in the same cluster as the query tile are considered as a partition. Figure 9 represents an example of such a partitioning application.

Although the accuracy of this approach is almost the same as the accuracy of the method that utilizes the homogeneous texture descriptor of MPEG-7 for similarity search (Manjunath et al., 2003), its processing time is about half of the other method. Specifically, if we develop such an application for an online system, that means feature extraction has to be performed prior to similarity matching in the online process, the total processing time of the proposed approach becomes less than one-third of the other method, which is quite significant.

V. CONCLUSION

This article presented an approach for image representation and retrieval using NLMDRT whose high efficiency in rotation-invariant image analysis has been already examined. We first efficiently extracted three major components of a texture, i.e., orientation, directionality, and regularity. Experimental results show that the proposed schemes for extraction of these components outperform previous works. We then developed a mechanism for image retrieval based on these components as well as the rotation-invariant texture feature. Experiments on a large number of images from standard datasets exhibit that the proposed approach has high accuracy in texture-based image retrieval applications.

Table V. Overall accuracy in N_{CAN} retrieved images for different weight settings based on relevance to textural classes.

	Weights	Accuracy in N_{CAN} (%)			
		20	40	60	80
1	$w_f = 1, w_d = 0, w_r = 0$	88.3	67.1	55.5	46.6
2	$w_f = 0.9, w_d = 0.05, w_r = 0.05$	89.8	68.2	56.6	47.7
3	$w_f = 0.8, w_d = 0.1, w_r = 0.1$	86.0	65.5	54.1	45.5
4	$w_f = 0.6, w_d = 0.2, w_r = 0.2$	71.1	55.4	45.1	39.6
5	Adaptive scoring, Eq. (22)	89.9	69.9	58.5	49.2

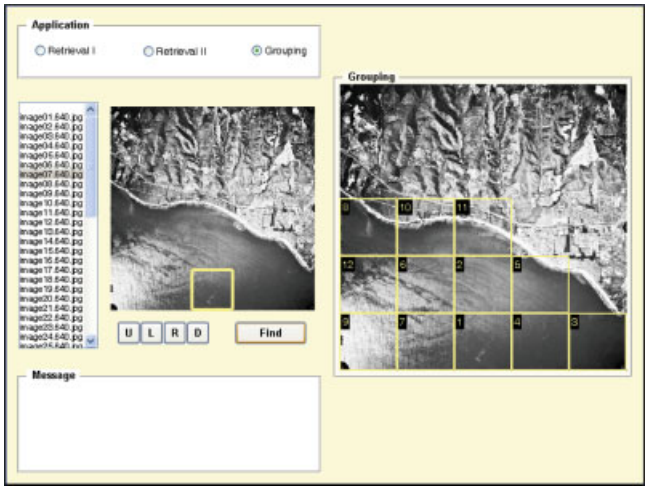

Figure 9. Example of partitioning of an aerial image. [Color figure can be viewed in the online issue, which is available at www.interscience.wiley.com.]

REFERENCES

J. Bigun, G.H. Granlund, and J. Wiklund, Multidimensional orientation estimation with applications to texture analysis and optical flow, IEEE Trans Pattern Anal Machine Intell 13 (1991), 775–790.

P. Brodatz, Texture: A photographic album for artists and designers, Dover, New York, 1966.

D.V.S. Chandra, Target orientation estimation using Fourier energy spectrum, IEEE Trans Aerospace Electron Syst 34 (1998), 1009–1012.

G.M. Haley and B.S. Manjunath, Rotation invariant texture classification using a complete space frequency model, IEEE Trans Image Process 8 (1999), 255–269.

M.R. Hejazi and Y.S. Ho, A hierarchical approach to rotation-invariant texture feature extraction based on Radon transform parameters, In 13th IEEE Conference on Image Processing (ICIP2006), Atlanta, USA, October 2006, pp. 1469–1472.

M.R. Hejazi and Y.S. Ho, Texture analysis using modified discrete Radon transform, IEICE Trans Inf Syst E90-D (2007), 517–525.

M.R. Hejazi, G. Shevlyakov, and Y.S. Ho, Modified discrete Radon transforms and their application to rotation-invariant image analysis, In Eighth IEEE Workshop on Multimedia Signal Processing (MMSP2006), Victoria, Canada, October 2006, pp. 429–234.

K. Jafari-Khouzani and H. Soltanianzadeh, Radon transform orientation estimation for rotation invariant texture analysis, IEEE Trans Pattern Anal Machine Intell 27 (2005), 1004–1008.

A. Jalil, I.M. Quareshi, A. Manzar, and R.A. Zahoor, Rotation-invariant features for texture image classification, In IEEE International Conference on Engineering of Intelligent Systems, Islamabad, Pakistan, April 2006, pp. 1–4.

K. Lee and L. Chen, An efficient computation method for the texture browsing descriptor of MPEG-7, Image Vision Comput 23 (2005), 479–489.

B. S. Manjunath, P. Salembier, and Th. Sikora, Introduction to MPEG-7, Wiley, New York, 2003.

B.S. Manjunath, P. Wu, S. Newsam, and H.D. Shin, A texture descriptor for browsing and similarity retrieval, Signal Process: Image Commun 16 (2000), 33–43.

R. Mester, Orientation estimation: Conventional techniques and a new non-differential approach,'' In 10th European Signal Processing Conference, Vol. 2, Islamabad, Pakistan, 2000, pp. 921–924.

C.M. Pun and M.C. Lee, Log-polar wavelet energy signatures for rotation and scale invariant texture classification, IEEE Trans Pattern Anal Machine Intell 25 (2003), 590–603.

A.W.M. Smeulders, M. Worring, S. Santini, A. Gupta, and R. Jain, Content-based image retrieval at the end of the early years, IEEE Trans Pattern Anal Machine Intell 22 (2000), 1349–1380.

H. Tamura, S. Mori, and T. Yamawaki, Texture features corresponding to visual perception, IEEE Trans Syst Man Cybernet SMC-8 (1978), 460–473.

VisTex: Vision Texture database, MIT Media Lab., http://vismod.media.mit.edu/vismod/imagery/VisionTexture/ (2002).

J. Zhang and T. Tan, Brief review of invariant texture analysis methods, Pattern Recognit 35 (2002), 735–747.